Journal of
Marine Science and Engineering

MDPI

Article

Pressure Hull Design Methods for Unmanned Underwater Vehicles

Alessia Meschini [1,2,*], Alessandro Ridolfi [1,2,*], Jonathan Gelli [1,2], Marco Pagliai [1,2] and Andrea Rindi [1,2]

[1] Department of Industrial Engineering (DIEF), University of Florence, Via di Santa Marta 3, 50139 Florence, Italy; jonathan.gelli@unifi.it (J.G.); m.pagliai@unifi.it (M.P.); andrea.rindi@unifi.it (A.R.)
[2] Interuniversity Center of Integrated Systems for the Marine Environment, Via all'Opera Pia, 13, 16145 Genova, Italy
* Correspondence: alessia.meschini@unifi.it (A.M.); a.ridolfi@unifi.it (A.R.)

Received: 4 September 2019; Accepted: 22 October 2019; Published: 28 October 2019

Abstract: This paper describes design methods for the plastic hull of an Unmanned Underwater Vehicle (UUV), with a particular focus on its cylindrical body and nearly spherical domes at the ends. With the proposed approach, the methodologies reported in the literature were compared, and suitable modifications and improvements were investigated and implemented to extend the classical theories and data to this case study. The investigated underwater vehicle, named FeelHippo, was designed and assembled by the Department of Industrial Engineering of the University of Florence. Its main hull is composed of an extruded PMMA (PolyMethyl MethAcrylate) cylinder and two thermoformed PMMA domes. Breakage of the hull results in destructive phenomena, namely, yielding and buckling. An experimental campaign and FEM (Finite Element Method) analysis were carried out to complete the theoretical study, and the collapse pressures were compared with the derived design values. In conclusion, the proposed innovative method is a lean and effective technique for designing underwater hull domes and predicting the collapse pressures.

Keywords: Unmanned Underwater Vehicles; Autonomous Underwater Vehicles; underwater vessel design; buckling; structural analysis; hull; collapse

1. Introduction

This paper compares collapse pressure prediction techniques in the literature and presents an innovative hull design strategy starting from an Autonomous Underwater Vehicle (AUV) developed by the Mechatronics and Dynamic Modelling Laboratory (MDM Lab) of the University of Florence. The study is based on theoretical checks, Finite Element Method (FEM) analysis, and experimental tests, and it aims to use the available data to extend the scope of the relationships established in the literature.

In the 1950s [1], the first ROV (Remotely Operated Vehicle) was developed for archaeological research, namely, the POODLE, and for military uses, namely, the Cable-Controlled Underwater Research Vehicle (CURV). Since then, there has been growing interest in the underwater environment and the development of Unmanned Underwater Vehicles (UUVs). The design of underwater vehicles is highly dependent on the sector that will implement it (e.g., [2–4]). The shape of the hull, a primary focus of the design, is most often cylindrical [5] or spherical. In underwater robotics [6], the more commonly used geometry is spherical rather than a flat surface because the distribution of stress on the surface is homogeneous, and the hydrodynamic drag is reduced. The hull material is another fundamental aspect to consider since the production process can introduce non-negligible peculiarities [7,8]. In this case, the use of PolyMethyl MethAcrylate (PMMA) as a material allows for an appropriate balance between

inexpensiveness, optical properties, and mechanical strength. Nevertheless, in the state-of-the-art literature, only a few studies have been conducted on thermoformed flanged domes, which usually have a shape that considerably differs from the ideal spherical shape as a direct result of the production process [9]. Our research objective is to study the problem of structural collapse for thermoformed flanged domes and to extend the classical theoretical formulations on structural collapse in the technical literature to this specific test case while considering the significant variation in the thickness [9,10] and aspect ratio, together with the constraints [11]. In the overall framework, the most common fields of application are submarine archaeology [12–15], oceanography [16], and inspections of underwater installations [17], such as those for Oil and Gas industries [18]. UUVs include different kinds of vehicles, such as Autonomous Underwater Vehicles (AUVs) and ROVs. The main difference is their operational mode: the first type is fully autonomous, while the second type is human controlled through a cable. Although the design methods for pressure hulls are generally valid for UUVs, the test case in this study focuses specifically on FeelHippo, which is an AUV developed by the Department of Industrial Engineering of the University of Florence.

The hull of underwater vehicles usually has a resistant structure that is capable of keeping the atmospheric pressure inside, as well as a coating structure with good hydrodynamic efficiency. Most submarine hulls have typical geometric structures [5], and this work particularly focuses on circular cylinders and domes. Domes are ideal for responding to external pressure because if ratios between the thickness of the wall and the diameter are small, then they allow for an almost uniform distribution of stresses through the thickness [19].

Both yielding and buckling can result in failures; their causes, which include geometry and boundary conditions, are highlighted below.

The first geometry of interest is the cylinder (such as the central hull of FeelHippo AUV): the ideal main structure is usually a cylindrical shell crossed with equidistant rings and end caps. The analytical studies found in the literature have considered the behavior of a cylindrical portion between two rings, and they have accounted for the simplification, uncertainties, and unmanageable details with appropriate safety coefficients. As a result of external pressure, a generic ductile resistant hull can be damaged in three ways, as visible in Figure 1: yielding, local instability, and general instability.

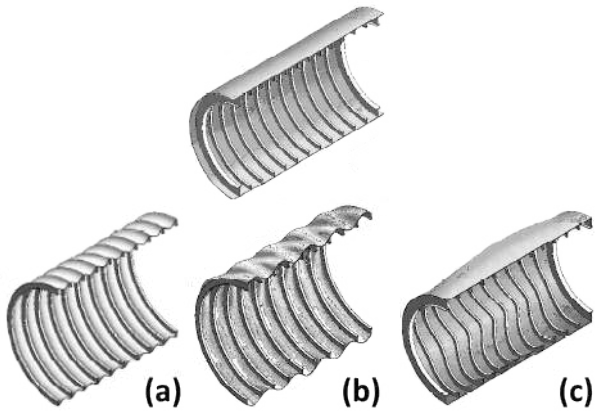

Figure 1. Cylindrical structure with non-deformed internal rings (on top), subjected to yielding (**a**), local instability (**b**), and general instability (**c**).

Yielding is axisymmetric inelastic, while local instability involves an asymmetrical inelastic collapse. The current trend of designing hulls of underwater vehicles is to consider a specific sizing so that only yielding can occur at the design pressure. Because appropriate safety coefficients are used, the critical factors linked to both local and general instability should appear after the operating pressure exceeds the design pressure. In particular, the failure modes due to global instability are very sensitive to manufacturing imperfections [20].

When the external pressure generates compressive stresses that reach high levels, instability buckling phenomena predominate. For basic geometries, the linear buckling load can be determined by analytical and numerical studies [21]. However, the linear buckling load is only an indication of the real buckling resistance of a shell; other important factors, such as geometric imperfections and the effects of the boundary conditions, must be considered [19] to obtain the actual buckling strength. For this reason, this study focused on breakage due to the instability of cylinders. Sizing is carried out to ensure that the structure will not be damaged, regardless of the phenomenon that occurs.

With the application of a uniform pressure range, the collapse of a circular cylinder occurs with an external pressure that is a small fraction compared with the internally applied pressure. This mode of failure is known as shell instability or lobar buckling, and it causes a collapse around its circumference in the form of a number of circumferential waves or lobes [22].

General instability manifests as the physical collapse of the entire shell because of the low strength of the ring-stiffeners. Finally, axisymmetric deformation takes place if the circular cylinder implodes while maintaining its circular shape [22]. Resistance to external pressure is further diminished by initial out-of-circularity [23].

The second geometric shape studied is the dome, which can collapse in different ways but presents a sudden loss of load capacity triggered by buckling. Studies on nonlinearity and marked imperfection sensitivity have been carried out since the study in [24]. Under a uniformly compressed state, both axisymmetric and asymmetrical behaviors can occur, as shown in [25]; in particular, the study focused on buckling and compression. These types of collapse are based on geometric and structural characteristics: for this reason, various breaking prediction theories have been studied to prevent these phenomena, as is the case in the present study. For this geometry, this study builds on the literature and represents a step forward in collapse prediction theories.

A hemispherical shell is able to withstand higher internal pressure than any other geometrical hull with the same wall thickness and radius. Thus, it is a major component of pressure vessel construction and has a smaller surface area per unit volume than any other shape. For complicated structures, such as shells, the modern design technique tends to improve the model investigation since, in most cases, the true behavior of the shell, with the load and the constraints, is not known or very difficult to know. The best approach is to make some assumptions and then verify them by using dedicated tests [26].

Although the literature reports numerous complex theoretical treatments, there is a lack of implementation in real and diverse applications [21], and there are few validations of the proposed theories. The cases presented in the state-of-the-art literature do not fit the results obtained herein (Section 5) because of the non-negligible discrepancy in the constraints and the production process (e.g., [7]). A similar problem, which was found to be inherent in the difficult task of associating a coefficient with a type of constraint, was discussed in [27].

Both the cylinder and domes investigated in this study are made of PMMA, so the objective of this work is also to adapt the classical methods to a different material and, above all, the production method. The most common materials for these types of mobile robots are metal alloys (high-strength steels, aluminum, or titanium) or composites (glass-fiber-reinforced plastic, carbon epoxy, or metal matrix composite) [4,28]. Furthermore, compared with the most common AUVs (e.g., REMUS-100 AUV [29], Fòlaga AUV [30], SPARUS II AUV [31], and Matsya 5.0 [3]), the shape of the designed vehicle investigated in this study is more compact and less torpedo-like.

This study focused on the autonomous vehicle called FeelHippo AUV [32] (shown in Figure 2, Section 2). First, the theoretical critical buckling pressure of the cylinder was calculated using classical formulas [33]; second, the critical buckling pressure was analytically derived and used to determine the optimized size in order to calculate the lowest thickness of the vehicle's central cylinder to address the buckling effect. The available domes were experimentally tested until breakage, and then the dome design pressures were obtained. As described below, additional correlations that were introduced resulted in good agreement between the theoretical results and both the FEM and experimental results.

An overall operational water depth of 30 m was determined. Finally, from the achieved results, a new restyled version of the vehicle was realized.

For the cylindrical geometry, both a theoretical comparison and a simulated validation were performed. The theoretical formulations in the literature were used for verification. The widely applied cylindrical geometry was used to approach the problem of collapse and allowed the research group to become familiar with the phenomenon. For the domes, first, an experimental campaign was carried out. Then, the theories available in the literature were studied: because the correspondence with the proposed case was not satisfactory, some improvements and additions were applied. The results obtained with the new proposed approach are encouraging and allow for the extension of the cases investigated in the literature. Furthermore, the dome geometry is widely used in the field of submarine robotics.

This paper presents the redesign of FeelHippo AUV, particularly its central hull—a cylinder and two flanged domes. The remainder of the paper is organized as follows: Section 2 illustrates the main mechanical and electronic characteristics of the vehicle. Section 3 focuses on the design of the cylindrical component by starting from theory and the state-of-the-art literature and ending with the investigated case and related validation. In Section 4, experimental tests on the dome are described, and Section 5 expands on the design of the domes by applying theoretical treatments and improvements to match the experimental evidence. Finally, Section 6 presents the conclusions and proposes some future developments.

The overall aim of this research is to create a simplified calculation system for the design and sizing of submarine hull parts under pressure and, in particular, to codify a fast and light computational procedure to check the resistance of cylinders and domes. A dedicated experimental campaign enabled the proposal of an extension of classical test cases in the literature, especially for the second geometry. The experimental campaign, in which the collapse of available domes was tested, facilitated the creation of a small dataset from which the theoretical equations were extended and validated. The main contribution of this research is the proposed design method to identify the mechanical resistance of the domes. For the sake of clarity, the classical theoretical theories and thus the FEM were based on the assumption of a perfect sphere, with only the stiffness of the material taken into account. In this work, the thickness variation and the flange constraints were introduced to consider the real shape of the dome and extrapolate suitable corrective coefficients. The proposed approach starts from the geometrical data and enables the identification of the failure mode and the reachable operational water depth.

2. Case Study: FeelHippo AUV

FeelHippo AUV, shown in Figure 2, is an AUV specially designed to be a development platform to test new payload and new control algorithms for both the MDM Lab research group and its students. This is reflected by the vehicle's involvement in several monitoring tasks and student competitions: SAUC-E (Student Autonomous Underwater Challenge—Europe) in both 2013 and 2016; Eurathlon in 2015; and ERL Emergency Robots in 2017 [34], 2018, and 2019. For this reason, the design specifications for the vehicle are very simple: light, cheap, small, and with an operating depth of a few meters. In the study reported in this paper, the real depth of immersion and navigation in safety were calculated and found to correspond to about 30 m.

The layout of the thrusters imparts FeelHippo AUV with an underactuated motion, with four marine propellers [35] controlling 4 degrees of freedom (DOFs) of the vehicle: two of these are mounted laterally in a V-shape to control the depth and the lateral movement (which is necessary for precise hovering); the other two are mounted in the backside on the horizontal plane, one per side, to control the motion along the longitudinal advancing direction and the yaw angle [36].

Figure 2. FeelHippo AUV.

The main structure of the vehicle is made of Anticorodal type 6082-T6 aluminum alloy and PMMA, commercially known as Plexiglas® (mechanical characteristics in Tables 1 and 2).

Table 1. Main mechanical characteristics of Anticorodal type 6082-T6 (EN AW-6082).

Property	Value
Density [kg/m^3]	2700
Yield strength [MPa]	260
Young's modulus [GPa]	68.9

Table 2. Main mechanical characteristics of PMMA (ISO 527-2).

Property	Value
Density [kg/m^3]	1180
Yield strength [MPa]	76
Young's modulus [GPa]	3.3

In Figure 3, a CAD of the vehicle is shown to highlight the overall dimensions.

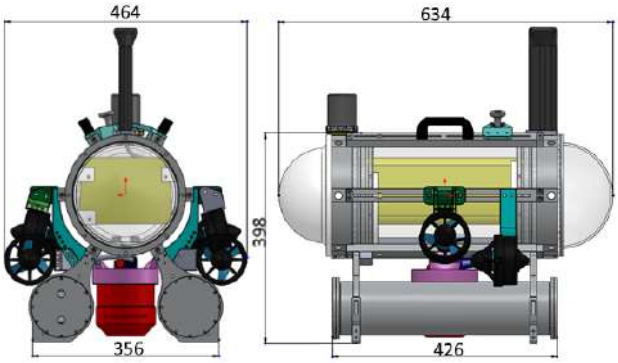

Figure 3. CAD design of FeelHippo AUV.

More details are shown in Figure 4. The vehicle's central body is a plexiglass tube containing the instrumental hardware, and Anticorodal type 6082-T6 constitutes the structural connections, and the two tubes under the main body house the batteries.

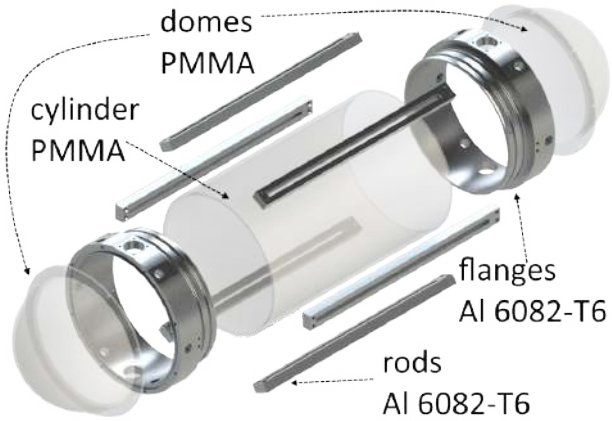

Figure 4. Main mechanical structure of FeelHippo AUV.

The body consists of an extruded cylinder and two flanged thermoformed domes. The thermoforming process entails heating a slab of material to 150–160 °C and then deforming it under vacuum by blowing without a counter-mold to maintain good optical quality. As discussed in Section 5, this implies that the thickness is variable and that the shape is not perfectly spherical.

The choice of materials was dictated by compromising between lightness, strength, and the ability to visually check the electronic components. Other external elements were printed in ABS (Acrylonitrile Butadiene Styrene) with a 3D printer from the MDM Lab (Stratasys Dimension Elite).

The differences between the selected materials had a profound influence on the design phase. In fact, the aluminum parts were sized to ensure structural resistance to impacts, which represent another type of possible failure. This choice also ensured that the aluminum parts could endure buckling instability: for this reason, given the difference in the thicknesses of the various elements, this work performed buckling optimization only for the PMMA components (also because this material has a much lower yield strength and Young's modulus). The PMMA domes and the main tube are connected by aluminum rods and flanges, which are equivalent to ring-stiffeners (Figure 4).

The FeelHippo design is thought to have limited roll and pitch angles during vehicle navigation. This feature is commonly adopted in AUV designs and is obtained by placing its center of gravity below its center of buoyancy. In this case, the AUV has a large and light main body, which contains the mainboards and other hardware, and two smaller and heavy legs, which contain the batteries and balancing weights.

In the electronic architecture, the main computer communicates with other devices by means of serial communication and an internal Ethernet network. Devices connected with serial communication are

- Radio modem to send short messages from high distances on the surface;
- GPS receiver on the surface to quickly localize the vehicle;
- FOG (Fiber Optic Gyroscope), a single-axis gyroscope with high precision to improve the pose estimation (particularly the yaw measurement);
- Custom board to monitor internal temperature; it also includes a water leakage sensor, battery SOC, and a control custom beacon flash and status LEDs;
- USB camera to provide frontal images during navigation;
- IMU (Inertial Measurement Unit) to provide data from the 3D internal accelerometer, gyroscope, and magnetometer;
- Acoustic modem, which enables a high data transfer rate (13.9 kbit/s) and a high functioning range (3500 m);
- Servo driver, an electronic board to control the four outrunner brushless motors.

The other devices, which are connected to each other in a cabled Ethernet network with two switches, are

- DVL (Doppler Velocity Log), which provides a 3-axial linear speed and altitude measure referred to the seabed using the Doppler effect and the depth of the vehicle by means of an integrated pressure sensor;
- WiFi AccessPoint, which allows for fast, high-band, short-range communication on the surface;
- 2D forward-looking sonar that allows the vehicle to see obstacles in situations of poor visibility;
- IP cameras to acquire images of the seabed and facilitate 3D reconstruction.

The energy supply that powers the vehicle comprises three LiPo batteries placed inside the aluminum pipes. In addition, other voltage levels are provided by dedicated DC/DC converters. The main voltage value lines are shown in Figure 5, along with the brands and models of the devices.

All these devices are largely in the main plexiglass body, stacked on two plastic planes. Only the IP cameras, 2D forward-looking sonar, and DVL are hung from the external structure.

Figure 5. Power supply for the onboard devices.

3. Design of the Main Cylinder of the AUV Hull

In this section, the equations for local instability are given. The critical buckling pressure equations were derived from the buckling analysis proposed both by R. Von Mises and by D.F. Windenburg and C. Trilling. Particular emphasis was placed on the case of submarines that have a circular cylinder, are closed at the ends, and are deeply submerged in water and thus exposed to pressure from all sides [37]. Since thin cylinders subjected to uniform external pressure collapse in an asymmetrical mode (lobar buckling), the local instability was studied at a fraction of the pressure needed to cause axisymmetric yielding.

Specifically, an analytical reference formulation for the study of short thin tubes that are supported at the ends and subjected to uniform radial and axial pressure was proposed. The formulation was subsequently modified by Von Mises [22]:

$$P_{crit} = \frac{Et}{R}\left[\frac{1}{n^2+\frac{1}{2}\left(\frac{\pi R}{L}\right)^2}\right]\left\{\frac{\left(\frac{\pi R}{L}\right)^4}{\left[n^2+\left(\frac{\pi R}{L}\right)^2\right]^2}+\frac{\left(\frac{t}{R}\right)^2}{12(1-\nu^2)}\left[n^2+\left(\frac{\pi R}{L}\right)^2\right]^2\right\} \quad (1)$$

$$P_{crit} = \frac{Et}{R}\left[\frac{1}{n^2-1+\frac{1}{2}\left(\frac{\pi R}{L}\right)^2}\right]\left\{\frac{\left(\frac{\pi R}{L}\right)^4}{\left[n^2+\left(\frac{\pi R}{L}\right)^2\right]^2}+\frac{\left(\frac{t}{R}\right)^2}{12(1-\nu^2)}\left[n^2-1+\left(\frac{\pi R}{L}\right)^2\right]^2\right\} \quad (2)$$

where
P_{crit} [MPa] = theoretical buckling pressure;
R [mm] = average cylinder radius;
t [mm] = wall thickness;
L [mm] = unsupported length of the cylinder;
E [MPa] = Young's modulus;
ν = Poisson's ratio;
n = number of circumferential waves lobes (an integer that minimizes the expression).

In a precautionary manner, the difference between the real scenario and the theoretical hypotheses was considered by introducing the corrective factor k [20].

$$P_{design} = kP_{crit} \quad (3)$$

where k varies according to t:
$k = 0.4$ for $t < 5$ mm
$k = 0.5$ for $5 < t < 7$ mm
$k = 0.6$ for $t > 7$ mm
P_{design} = operative pressure at which the vehicle can dive and navigate safely.

The following expression, proposed by D.F. Windenburg and C. Trilling, does not depend on the number of lobes [23]:

$$P_{crit} = \frac{2.42E}{(1-\nu^2)^{\frac{3}{4}}}\left[\frac{\left(\frac{t}{2R}\right)^{\frac{5}{2}}}{\frac{L}{2R}-0.45\left(\frac{t}{2R}\right)^{\frac{1}{2}}}\right] \quad (4)$$

Its result differs by a maximum of 3.5% from the result of Von Mises's formulation, so it is sufficiently accurate for practical applications.

Ross presented a comparison between the theoretical models, the experimental results, and simulated results [21]. For instance, Figure 6 reports the results for an Anticorodal 6082-T6 tube with the outer diameter $2R + t = 50$ mm and $t = 1.7$

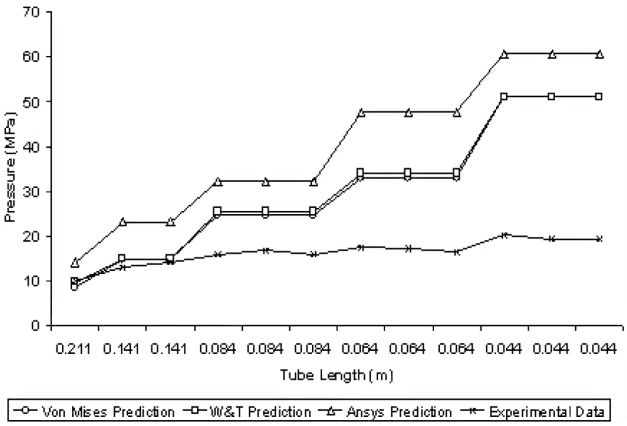

Figure 6. Predicted buckling pressure versus tube length [23].

The literature also includes graphs to calculate the pressure that is actually bearable by the cylinder according to its geometric characteristics and its material. The calculations are based on both a theoretical basis and experimental results; therefore, the results are even more reliable. Figure 7 presents a design chart for thick-walled circular cylinders that collapse under external hydrostatic pressure [22].

$$\lambda_c = \left[\frac{\left(\frac{L}{2R}\right)^2}{\left(\frac{t}{2R}\right)^3} \right]^{\frac{1}{4}} \left(\frac{\sigma_y}{E}\right)^{\frac{1}{2}} \tag{5}$$

$$PKD = P_{crit} / P_{exp} \tag{6}$$

where
σ_y [MPa] = yield strength;
λ_c = slenderness of the cylinder;
P_{exp} [MPa] = the experimentally obtained buckling pressure, which is ultimately an intermediate value between the theoretical and safety pressures and specifies the pressure at which the vehicle could start collapsing;
PKD = Plastic Knock Down factor, the ratio between the theoretical and experimental pressures.

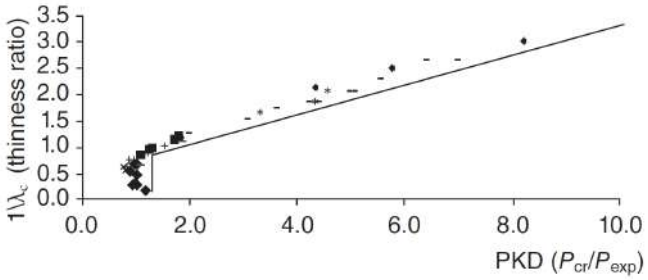

Figure 7. Design chart for the shell instability of machined circular cylinders [21].

In addition, a safety coefficient (SF) $<$ 3 e.g., arbitrarily 1.5 is added to obtain the real design operative pressure (a value of 3 is used for the case in which people are onboard). It can be seen that if $1/\lambda_c < 0.9$, the structure will probably fail by elastic instability, followed by axisymmetric deformation. Additionally, there is a link between plastic axisymmetric deformation and inelastic shell instability.

$$P_{design} = \frac{P_{exp}}{SF} \tag{7}$$

The ability to withstand pressure is reduced if the cylinder is manufactured with an initial out-of-circularity. Comparing experimental and theoretical data reveals that as the length of the cylinder decreases, the theoretical data deviate from the experimental evidence (Figure 6) because of edge effects, too. Therefore, corrective factors are needed to ensure a certain safety margin.

For the geometry of FeelHippo AUV, in accordance with the aforementioned nomenclature, the cylinder data are summarized in Table 3.

Table 3. Geometrical cylindrical data.

R [mm]	t [mm]	L [mm]	E [MPa]	ν
107.5	5	272	3300	0.39

First, the theoretical critical buckling pressure (the pressure at which the hull would collapse under ideal conditions) was calculated.

Table 4 summarizes the theoretical pressure for the case under examination: the first two columns identify the cylindrical thickness and the number of lobes; the third column reports the values from Equation (1), the fourth column reports the values from Equation (2), the fifth column reports the values from Equation (4), and the last column reports the results of the FEM analysis described below. The values are quite similar among the various formulations.

Table 4. Theoretical buckling pressure values.

t [mm]	n	Von Mises Equation (1) [MPa]	Von Mises Equation (2) [MPa]	Windenburg Trilling Equation (4) [MPa]	FEM [MPa]
5	4	0.67	0.64	0.62	0.64

The necessary geometry was obtained by carrying out sizing optimization to perform an FEM comparison and an evaluation of the minimum volume of material—that is, the minimum thickness of the cylinder to withstand the calculated pressure, less than 0.7 MPa. As a result, the axial load was imposed on the frontal section while a uniform external pressure was applied to the structure. The first thickness was set to 10 mm to avoid influencing the test.

The FEM results of the sizing optimization analysis by HyperMesh are shown in Figure 8 (static pressure) and Figure 9 (qualitative, first buckling mode). After several iterations, the solver identified a minimum necessary thickness of 5.08 mm, which can be reasonably approximated to 5 mm.

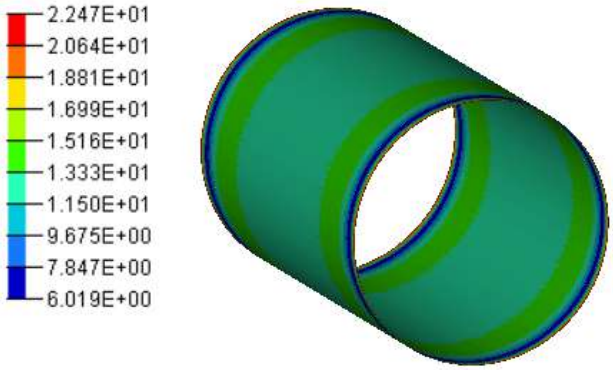

Figure 8. Optimized cylinder stresses (MPa) due to static pressure, 0.7 MPa.

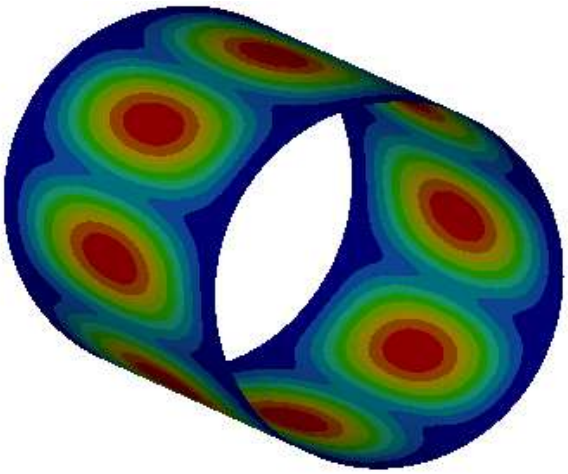

Figure 9. Optimized cylinder first buckling mode, n = 4, using HyperMesh.

Figure 10 shows a qualitative representation of the results of the FEM analysis using SOLIDWORKS. Both ends are interlocked to simulate the behavior of the rods. A tetrahedral solid automesh was chosen, with 7593 elements and 15,437 nodes.

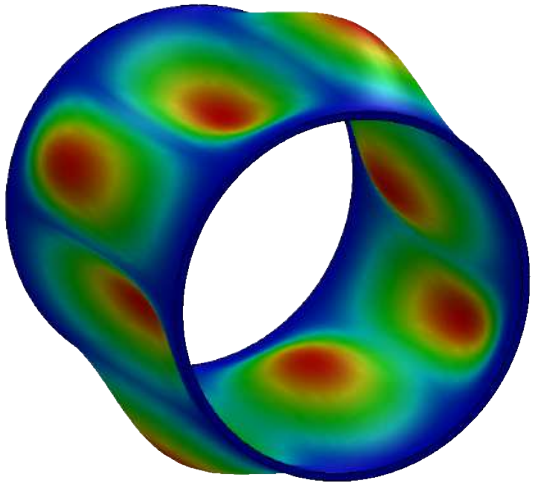

Figure 10. Optimized cylinder first buckling mode using SOLIDWORKS.

There is a complete match between the results of the FEM analysis and the theoretical results derived from Von Mises's theory. The number of circumferential lobes is 4, which is in agreement with both Equations (1) and (2).

The last step includes the derivation of the real critical buckling pressure by using both the classical and experimental methods. In sum, the first method uses the theoretical value of the pressure derived by R. Von Mises' or D.F. Windenburg and C. Trilling's equations, with corrections applied by using the corrective factor k. The second (experimental) method corrects the theoretical value through experimental charts (λ_c and PKD) and the safety coefficient SF. From the chart in Figure 7, it is possible to calculate the coefficient λ_c, particularly $\lambda_c = 2.87$ (Equation (5)), to find the value of $PKD \simeq 1.3$ and, consequently, $P_{exp} = 0.49$ MPa (Equation (6)), which is the experimental bearable pressure value. Using a safety factor (Equation (7)) $SF = 1.5$, the design pressure $P_{design} = 0.32$ MPa (about 30 m) is obtained. This is the same value that results from using the safety coefficient $k = 0.5$ and P_{crit} of Equation (1) in Equation (3).

In conclusion, the operative depth obtained for the case under examination is about 30 m.

A theoretical investigation was also carried out for other cases that have been tested by other researchers [38]; this renders the validation more credible if the same results are obtained. Table 5

summarizes the buckling pressure data found: specifically, it presents the geometric data of the two aluminum tubes tested by BlueRobotics, their experimentally detected critical buckling pressures, and finally, the theoretical results derived from the FEM analysis and Equation (1). The number of lobes is the same in each of the three cases. It is reasonable to assume that the tested cylinders are almost free from imperfections in addition to having an excellent geometric ratio.

Table 5. Comparison with BlueRobotics data [38].

R [mm]	t [mm]	L [mm]	Experimental Collapse [MPa]	FEM [MPa]	Von Mises Equation (1) [MPa]	n
43.45	2	180	7.5	7.25	7.55	3
55.95	2.4	239	6.1	5.91	6.11	3

4. Experimental Tests on Domes

Some experimental tests were carried out in the MDM Lab pressure chamber, as shown in Figure 11. The technical characteristics of the pressure chamber are

- material: high-strength steel;
- operating fluid: freshwater;
- dimensions: horizontal length of 2 m and diameter of 400 mm;
- maximum working pressure: 35 bar.

Figure 11. MDM Lab pressure chamber.

Each component, that is, each dome with different features, was tested together with other more resistant components to avoid influencing the test with other collapses. Each test was performed three times, and the same result was obtained in each trial:

- two domes were held together by 8 screws, divided by a protective flat seal (Figure 12);
- the hydrostatic pressure was raised step by step and maintained;
- the collapse pressure was detected using the manometer (just near the buckling collapse in Figure 13);
- after depressurization, each element was checked (Figure 14 shows an example of yielding collapse occurring close to the flange).

Figure 12. Example of two joined domes before testing.

Figure 13. Pressure chamber manometer.

Figure 14. Check of breaking mode.

The obtained results are summarized in Table 6 (t_s denotes the nominal thickness of the slab, R denotes the mean radius, h denotes the height of the dome, and R_f is the external radius of the flange).

Table 6. Dome experimental data.

t_s [mm]	h [mm]	R [mm]	R_f [mm]	Experimental Collapse [MPa]	Predominant Phenomenon
3	98	97.75	230	0.22	buckling
6	95	96.25	230	1.35	yielding
10	91	95.75	230	1.45	yielding

5. Design of Domes

It has been observed that the dome geometry can collapse in different manners depending on certain parameters. First, two equations from the literature are reported [24,39,40].

The first equation calculates P_{crit}, the theoretical critical buckling pressure for a thin sphere:

$$P_{crit} = \frac{2Et_s^2}{R^2\sqrt{[3\,(1-\nu^2)]}} \tag{8}$$

The second equation is related to the critical static compression pressure (based on large-deformation theory of shells) that causes membrane yield in the sphere (P_c):

$$P_c = 0.365E\left(\frac{t_s}{R}\right)^2 \tag{9}$$

Since these equations represent two different failure modes, each one is valid for a specific field of application, and it is worth noting that their results could not be the same. Compared with the previous notation, it is important to highlight that

R [mm] = the radius of the hemisphere to mid-thickness;
t_s [mm] = the nominal dome thickness;

and, as before,

E [MPa] = Young's modulus;
ν = Poisson's ratio.

As one might expect, a hemispherical dome has a better buckling resistance than other kinds of domes. Indeed, hemi-ellipsoidal prolate and hemi-ellipsoidal oblate domes are ten times less robust than hemispherical domes. Experimental tests [21] have shown that the structural failure of domes occurs for values of critical pressure lower than those theoretically predictable by the formulas above. The literature reports many specific correlations but only for very limited fields of application [6]. The aim of this work is to extend the field of application of the available values.

The comparison between the theoretical data and the experimental data from the previous section is not satisfactory (Table 7). Hence, there is a need to introduce corrections to predict the behavior of the case under study. This process starts from the theoretical critical buckling pressure of a hemispherical dome (P_H) and the ideal yield pressure for hemispherical and homogeneous domes (P_y). In this study, the variation in thickness, the aspect ratio, and the type of constraint were taken into account, given their non-negligible influence.

Table 7. Comparison between experimental and theoretical data found in the literature.

t_s [mm]	Experimental Collapse [MPa]	P_{crit} (Equation (8)) [MPa]	P_c (Equation (9)) [MPa]
3	0.22	3.90	1.13
6	1.35	16.08	4.68
10	1.45	45.14	13.14

The collapse pressures obtained from experimentation are generally less than those calculated using theoretical formulas because of the geometric imperfections. Furthermore, in the case studied, the geometry strongly depends on the manufacturing method.

The chosen domes are made of plastic by thermoforming. The structural characteristics of the objects realized in this type of production process vary according to the geometric characteristics, and they differ considerably from those produced by other production techniques.

Unfortunately, therefore, the experimental theories derived from case studies in the literature [21,41], although suitable for highly regular domes, cannot be directly applied to thermoformed PMMA. Thus, the theories and equations were modified, verified, and compared with the results of the FEM analysis.

In the flange part, the thickness, t_s, is the nominal thickness of the plexiglass plate, but the thickness decreases as it approaches the center of the dome, as shown in the chart in Figure 15. Hence, for safety, the thickness used is t_H, which is the minimum of the dome (to clarify, in Table 8, the geometrical data are as follows: R is the mean radius, h is the height of the dome, and d is the external radius of the dome; all three variables do not consider the flange). The blue dotted line is the interpolation performed in this study (Equation (10)) [42].

$$\frac{S_2}{S_1} = s_4 + \frac{s_1 - s_4}{1 + \left(\frac{\frac{h}{d}}{s_3}\right)^{s_2}} \tag{10}$$

where S_1, S_2, h, and d are geometrical quantities and shown in Figure 15; $S_1 = t_s$ and $S_2 = t_H$; and s_1, s_2, s_3, and s_4 are interpolation coefficients ($s_1 = 0.993$, $s_2 = 2.224$, $s_3 = 0.454$, and $s_4 = -0.224$).

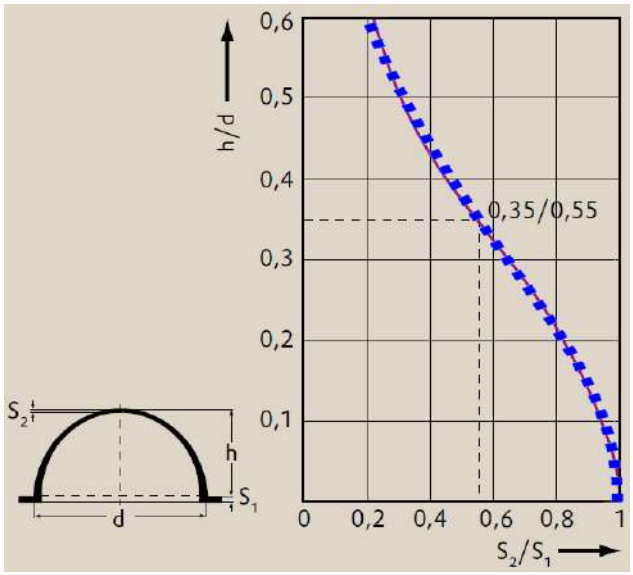

Figure 15. The thickness of a dome produced by blowing depends on the height/ratio.

Table 8. Geometrical data.

t_s [mm]	R [mm]	h [mm]	d [mm]	t_H [mm]
2	98.25	99	199	0.64
3	97.75	98	199	0.99
4	97.25	97	199	1.34
5	96.75	96	199	1.71
6	96.25	95	199	2.10
7	96.25	94	199	2.50
8	95.75	93	199	2.91
9	95.75	92	199	3.34
10	95.75	91	199	3.79

If the changes in the parameters are considered to be independent of each other in the first approximation, then the variation in the geometry, thickness, and constraints can be analyzed.

It has been observed that an imperfectly spherical shape influences the mode of dome breakage: as the thickness increases, the influence of the membrane buckling behavior decreases and favors

yielding, while the point of breakage moves from the top of the dome to the flanged base, close to the constraint. Furthermore, in the thickest domes, the radius of the inner curvature between the dome and the flange greatly influences its breaking behavior under compression, but this geometric parameter depends on the thermoforming process and thickness: the greater the thickness, the greater the radius and, consequently, the greater the mechanical stresses of the section. This is because the dome tends to overturn. On the other hand, as the radius of the external curvature between the flange and the dome decreases, local tensions increase. This justifies a sublinear trend. Other differences, which are discussed in the following part, are the AR (aspect ratio), distance from the unit, the presence of holes in the flange, and an imperfect hemisphere.

The purpose of this study is to derive a simplified and efficient method for the case under study and integrate the problems related to the aspect ratio and constraints into the calculation to identify the limit between compression and buckling.

The formulation of the theoretical critical buckling pressure (Equation (8)) can be corrected using the AR (R/h), which is dependent on the parameters of the dome and non-negligible in this particular case.

In Figure 16, a graph from the literature is given in which the colored dotted lines represent the interpolation performed in this study. Below are the relationships used to interpolate the graph. First is the initial linear part (based on a linear function) (Equation (11)); second is the nonlinear part (based on the power curve) (Equation (12)), and third is the scaling based on R/t_H (based on symmetrical sigmoidal) (Equation (13)).

$$\left(\frac{P}{P_H}\right)_k = f_k\left[l_1\left(\frac{A}{B}\right) + l_2\right] \tag{11}$$

with $l_1 = 1.286$ and $l_2 = -0.286$;

$$\left(\frac{P}{P_H}\right)_k = f_k\left[n_1\left(\frac{A}{B}\right)^{-n_2} + n_3\right] \tag{12}$$

with $n_1 = 2133.399$, $n_2 = -0.000198$, and $n_3 = -2132.389$;

$$f_k = q_4 + \frac{q_1 - q_4}{1 + \left(\frac{\frac{R}{t_H}}{q_3}\right)^{q_2}} \tag{13}$$

with $q_1 = 214528.5$, $q_2 = 0.969$, $q_3 = 0.00016$, and $q_4 = -0.041$.

In the above equations, l_1, l_2, n_1, n_2, n_3, q_1, q_2, q_3, and q_4 are interpolation coefficients; A/B is the aspect ratio in Figure 16, with $R = A$ and $B = h$; P_H is the theoretical critical elastic buckling pressure of a hemispherical dome (Equation (8), with t_H); and P is the theoretical critical buckling pressure for a non-hemispherical dome.

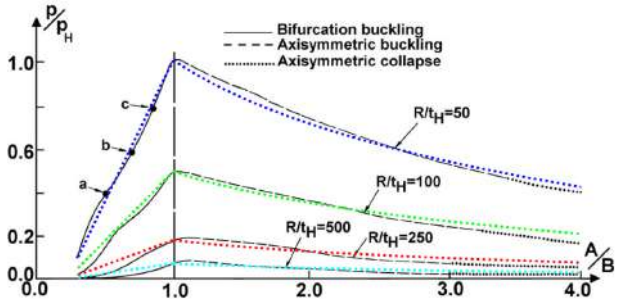

Figure 16. Elastoplastic buckling loads for different thickness ratios of the reference hemisphere [43] (AR = 1).

As regards the border between compression and buckling behavior, the parameter λ_d is considered. Starting from the state-of-the-art literature [44], λ_d (Equation (14)) expresses a ratio between pressures and a relationship between geometric and material features.

$$\lambda_d = \sqrt{\frac{P_y}{P_H}} = \sqrt{\left(\frac{R}{t_H}\right)\left(\frac{\sigma_{yield}}{E}\right)\sqrt{3\left(1-\nu\right)}} \tag{14}$$

where P_y = ideal yield pressure of hemispherical and homogeneous shell.

$$P_y = 2\left(\frac{t_H}{R}\right)\sigma_{yield} \tag{15}$$

From the experimental results, it was observed that if $\lambda_d < 1$ (Equation (15) is valid), then the rupture occurs because of the static compression load. On the other hand, if $\lambda_d > 1$, then the buckling phenomenon occurs (Equation (8) is valid).

It is highlighted that the mechanics of the fracture depend on the type of constraint, the material, its stiffness, and the specific production method.

For example, with consideration of only the constraint, in the particular case under examination, there are holes for connecting screws, and a peak of stress in their surroundings causes a crack and a brittle break that promote the initiation of the collapse.

A corrective factor is introduced (f_y) to take into account these effects. In this way, the theoretical corrected pressure (P_{yc}) matches the experimental one. The correction factor is based on a power curve Equation (16) derived from FEM analyses, and it is dependent on the dome thickness.

$$f_y = y_1 {t_s}^{y_2} \tag{16}$$

$$P_{yc} = \frac{P_y}{f_y} \tag{17}$$

with $y_1 = 0.383$ and $y_2 = 1.034$.

The influence of the correction of the coefficient λ_{dc}, which is the same as λ_d but with corrected pressures, follows a square root law, while the coefficient f_y follows a linear one. Therefore, the transition point of collapse is also affected. As a result of applying this coefficient, the theoretical data coincide with the experimental evidence, as summarized in Table 9.

Table 9. Comparison between theoretical and experimental data.

		Buckling			Yielding			
t_s [mm]	Exp [MPa]	P_H [MPa]	AR	P [MPa]	P_y [MPa]	f_y	P_{yc} [MPa]	λ_{dc}
3	**0.22**	0.42	1.00	**0.21**	1.53	1.19	1.29	1.75
6	**1.35**	1.97	0.99	2.16	3.31	2.45	**1.35**	0.86
10	**1.45**	6.48	0.95	12.66	6.02	4.15	**1.45**	0.49

Obviously, similar to the case with the cylinder, a safety factor for the dome (e.g., $SFd = 1.25$) has to be considered to obtain the pressure design. This starts from the minimum pressure between $P_{designDY}$ for yielding and $P_{designDB}$ for buckling, the pressure at which the vehicle could dive safely.

$$P_{designDY} = \frac{P_{yc}}{SFd}; P_{designDB} = \frac{P}{SFd} \tag{18}$$

As discussed, FEM analysis was performed, although with different thicknesses from those experimentally tested (Table 10), to both validate the proposed relationships of buckling pressure and delineate the correction curve for theoretical compression breakage (in the column of the FEM analysis results, only the real collapse pressure is reported; it is a sublinear trend, as is the experimental one). Given the difficulty of identifying the yielding breaking state, a system of constraints suitable for the case under examination was to set up by using experimental data. In particular, the static analysis of the 10 mm thick dome is reported in Figure 17. The results of the intermediate domes were used to define the corrective relationship. The bolts in stainless steel AISI 316, A470 EN ISO 3506, were inserted as connectors and simulated with their pretension clamping force set to 3760 N, which is equivalent to nominal tightening. The lower face of the flange was fixed, while the contact between the dome and the flange was imposed without penetration and with a friction coefficient of 0.5. A tetrahedral solid curvature-based mesh was chosen, with 202,760 elements and 317,983 nodes.

Table 10. Comparison between theoretical and FEM data.

	Experimental	Buckling		Yielding	
t_s [mm]	Collapse [MPa]	FEM [MPa]	P [MPa]	FEM [MPa]	P_{yc} [MPa]
2	-	**0.04**	**0.06**	-	1.27
3	**0.25**	**0.22**	**0.21**	-	1.29
4	-	**0.55**	**0.55**	-	1.31
5	-	**1.17**	**1.16**	-	1.33
6	**1.35**	-	2.16	**1.35**	**1.35**
7	-	-	3.62	**1.38**	**1.38**
8	-	-	5.82	**1.41**	**1.41**
9	-	-	8.75	**1.43**	**1.43**
10	**1.45**	-	12.66	**1.45**	**1.45**

The minimum theoretical value between buckling and yielding collapse pressures are in bold and stress the type of break, and the result is the same as the experimental result. Specifically, the collapse occurs because of buckling up to a thickness of 5 mm; beyond this thickness, the collapse is due to yielding.

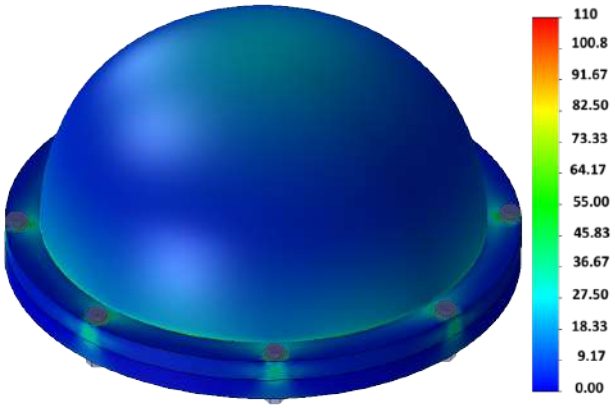

Figure 17. Dome stresses (Von Mises [MPa]) due to static pressure (1.45 MPa) for a thickness of 10 mm.

The most significant comparisons of breakage examples are qualitatively reported, and the experimental and FEM results match. In Figure 18, the intermediate (6 mm thick) domes broke in the lowest part because of the yielding phenomenon, and in Figure 19, the thinnest (3 mm thick) domes broke because of membrane buckling in the highest region.

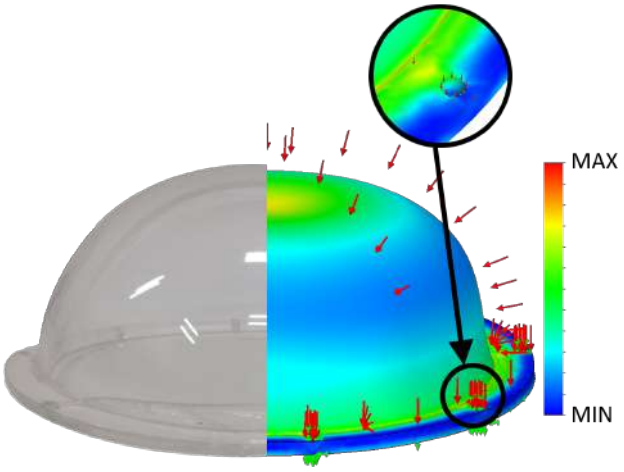

Figure 18. Compression rupture.

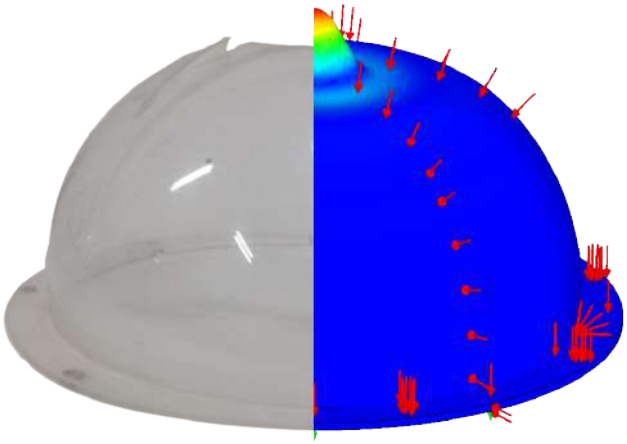

Figure 19. Buckling collapse.

Notably, both the real and the simulated domes are not perfectly hemispherical. With this corrected shape, simulations can be used to predict the real breaking position, as well as the collapse pressure. This characteristic depends directly on the thermoforming process. Moreover, the AR factor and radius of the curvature are very important for numerically reproducing its behavior.

The FEM results well reproduce the experimental data; consequently, they are considered reliable.

In the end, given the correlations reported, a 10 mm thick dome for our vehicle FeelHippo AUV was designed, as shown in Figure 20, in which the left shows the real dome, and the right shows the design chart. The vehicle is thus able to reach a depth of 30 m safely (the less resistant structural component is the cylinder).

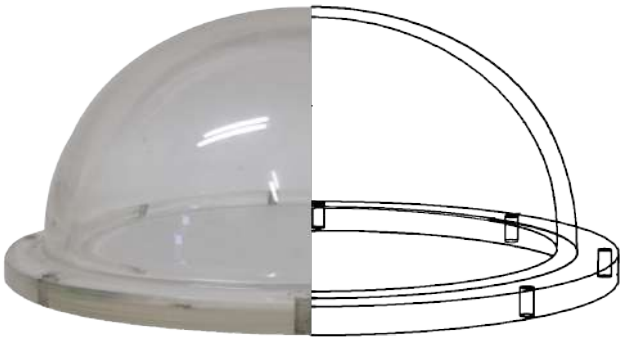

Figure 20. Dome designed for FeelHippo.

6. Conclusions and Future Developments

This paper presents theoretical and experimental investigations to produce a consistent relationship between both the classic naval design and innovative methods. A good correspondence between the experimental evidence and the optimized simulations is reported.

Regarding the design of the cylindrical tube, the geometry has been widely studied, and the related theory has been largely used; therefore, it is possible to effectively design the component in PMMA, too, even without using FEM analysis in the initial project step.

On the other hand, for the dome geometry, the standard theoretical approach is too generalized, and the specific results are influenced by boundary conditions, such as geometry and the linking constraints. Therefore, the predictive capacity of the algorithms was improved by using the available data in the literature to propose and introduce some correction coefficients. With the coefficients applied, the obtained results are very satisfactory.

Furthermore, because of the buckling instability phenomenon, the formula for sizing the dome was combined with the aspect ratio factor. This was implemented because the high region of the dome is affected by this kind of break, and the breaking mode largely depends on the geometry. The other formula predicts the compression break, which occurs in the area of the dome closest to the constraint. Given the strong dependence on the type of constraint and the production methodology of the dome, which even determines the radii of curvature at the base, an overall coefficient was identified for the specific case of a thermoformed plastic flanged dome fixed to the rest of the vehicle by screws.

As a result of the changes made, structural resistance to buckling and compression seems to be provided in an effective and correct manner for the specific case under study. The new dome was tested, and the results are encouraging.

Possible future developments are related to the evaluation of specific coefficients for each application, individual variation in the thickness, the constraint, and the manufacturing process. This requires a much broader experimental campaign that allows each of the many coefficients to be studied separately. Because of the costs of shell buckling experiments, the effects of the large number of variables to be considered could be analyzed first by a combination of experimental and numerical approaches.

For the thermoforming process, it could also be determined whether it is possible to define an equivalent thickness, starting from the original thickness and taking into account the production method, for other types of plastic material. Finally, the ultimate goal will be to develop a general method and extend it to different applications.

Author Contributions: conceptualization, A.M., M.P., and J.G.; methodology, A.R. and J.G.; software, A.M. and M.P.; validation, A.M., M.P., and J.G.; investigation, A.M. and J.G.; writing—original draft preparation, A.M.; writing—review and editing, A.R.; supervision, A.R.

Funding: This research received no external funding.

Conflicts of Interest: The authors declare no conflict of interest.

Notation

d	[mm]	External radius of the dome
f_y		Corrective factor for the theoretical yield pressure
h	[mm]	Height of the dome
k		Theoretical buckling pressure corrective factor dependent on the cylinder thickness
n		Number of circumferential waves lobes (integer that minimizes the expression)
t	[mm]	Wall thickness of the cylinder
t_H	[mm]	Minimum thickness of the dome
t_s	[mm]	Nominal thickness of the starting slab for dome geometry

AR		Aspect Ratio
E	[MPa]	Young's modulus
L	[mm]	Unsupported length of the cylinder between two reinforced rings
P	[MPa]	Theoretical critical buckling pressure for a non-hemispherical dome
P_c	[MPa]	Critical static compression pressure for a sphere
P_{crit}	[MPa]	Theoretical buckling pressure
P_{design}	[MPa]	Operative pressure at which the cylinder can dive safely
$P_{designDY}$	[MPa]	Operative pressure at which the dome can dive safely for yielding
$P_{designDB}$	[MPa]	Operative pressure at which the dome can dive safely for buckling
P_{exp}	[MPa]	Experimentally obtained buckling pressure at which the cylinder could start collapsing
P_H	[MPa]	Theoretical critical elastic buckling pressure of a hemispherical dome, considering t_H
P_y	[MPa]	Ideal yield pressure for hemispherical and homogeneous shells
P_{yc}	[MPa]	Theoretical corrected yield pressure for a hemispherical dome
PKD		Plastic Knock Down factor: ratio between the theoretical and experimental pressure
R	[mm]	Average radius
R_f	[mm]	External radius of the flange
SF		Safety coefficient for the cylinder
SFd		Safety coefficient for the dome
λ_c		Slenderness of the cylinder
λ_d		Slenderness of the dome
ν		Poisson's ratio
σ_y	[MPa]	Yield strength

References

1. Chris, R.D.; Wernli, R.L., Sr. *The ROV Manual. A User Guide for Observation Class Remotely Operated Vehicles*, 1st ed.; Elsevier: Amsterdam, The Netherlands, 2011.
2. Alam, K.; Ray, T.; Anavatti, S.G. A new robust design optimization approach for unmanned underwater vehicle design. *Proc. Inst. Mech. Eng. Part M J. Eng. Marit. Environ.* **2012**, *226*, 235–249. [CrossRef]
3. Mittal, V.; Dhakad, S.; Tyagi, K.; Prakash, J.; Kumar, A.; Bhagat, Y.; Singh, A.; Bakshi, S.; Verma, A.; Sharma, D.; et al. Research and Development of Matsya 5.0, Autonomous Underwater Vehicle. 2017. Available online: http://www.robonation.org/sites/default/files/RS17_IITB_Paper.pdf (accessed on 22 May 2018).
4. Ross, C.T.F. A conceptual design of an underwater vehicle. *Ocean Eng.* **2006**, *33*, 2087–2104. [CrossRef]
5. Deepika, K.R.; Kumar, N.J. Design optimisation of a pressure hull for dynamic loading. *Int. J. Eng. Sci. Innov. Technol.* **2013**, *2*, 562–586.
6. Krishnamachari, S.I.; Broutman, L.J. A design procedure for large spherical domes under external pressure. *J. Reinf. Plast. Compos.* **1997**, *16*, 1342–1349. [CrossRef]
7. Breddermann, K.; Drescher, P.; Polzin, C.; Seitz, H.; Paschen, M. Printed pressure housings for underwater applications. *Ocean Eng.* **2016**, *113*, 57–63. [CrossRef]
8. Jebelli, A.; Yagoub, C.; Dhillon, S. Design and Implementation of an Autonomous Underwater Vehicle (AUV) with PTFE. *Adv. Robot. Autom.* **2018**, *7*, 185.
9. Lai, M.O.; Holt, D.L. Thickness variation in the thermoforming of poly (methyl methacrylate) and high-impact polystyrene sheets. *J. Appl. Polym. Sci.* **1975**, *19*, 1805–1814. [CrossRef]
10. Ewing, P.D.; Williams, J.G. The fracture of spherical shells under pressure and circular tubes with angled cracks in torsion. *Int. J. Fract.* **1974**, *10*, 537–544. [CrossRef]
11. Wunderlich, W.; Albertin, U. Buckling behaviour of imperfect spherical shells. *Int. J. Non-Linear Mech.* **2002**, *37*, 589–604. [CrossRef]
12. Bingham, B.; Foley, B.; Singh, H.; Camilli, R.; Delaporta, K.; Eustice, R.; Mallios, A.; Mindell, D.; Roman, C.; Sakellariou, D. Robotic tools for deep water archaeology: Surveying an ancient shipwreck with an autonomous underwater vehicle. *J. Field Robot.* **2010**, *27*, 702–717. [CrossRef]
13. Allotta, B.; Pugi, L.; Bartolini, F.; Costanzi, R.; Ridolfi, A.; Monni, N.; Gelli, J.; Vettori, G.; Gualdesi, L.; Natalini, M. The THESAURUS project, a long range AUV for extended exploration, surveilance and monitoring of archeological sites. In Proceedings of the V International Conference on Computational Methods in Marine Engineering ECCOMAS MARINE 2013, Hamburg, Germany, 29–31 May 2013; pp. 760–771.

14. ARROWS Project. 2015. Available online: http://www.arrowsproject.eu/ (accessed on 22 May 2018).
15. Johnson-Roberson, M.; Bryson, M.; Friedman, A.; Pizarro, O.; Troni, G.; Ozog, P.; Henderson, J.C. High-resolution underwater robotic vision-based mapping and three-dimensional reconstruction for archaeology. *J. Field Robot.* **2017**, *34*, 625–643. [CrossRef]
16. Smith, S.M.; Dunn, S.E.; Hopkins, T.L.; Heeb, K.; Pantelakis, T. The application of a modular auv to coastal oceanography: Case study on the ocean explorer. In Proceedings of the Challenges of Our Changing Global Environment, Conference OCEANS'95 MTS/IEEE, San Diego, CA, USA, 9–12 October 1995; pp. 1423–1432.
17. Jacobi, M. Autonomous inspection of underwater structures. *Robot. Auton. Syst.* **2015**, *67*, 80–86. [CrossRef]
18. Jamieson, J.; Hopkins, D. The potential benefits autonomous underwater vehicles bring to subsea inspection in Arctic regions. In Proceedings of the OTC Arctic Technology Conference, Offshore Technology Conference, Copenhagen, Denmark, 23–25 March 2015.
19. Carvelli, V.; Panzeri, N.; Poggi, C. Buckling strength of GFRP under-water vehicles. *Compos. Part B* **2001**, *32*, 89–101. [CrossRef]
20. Marinò, A. *Mezzi Sottomarini—Appunti del Corso di Navi Militari e Sommergibili*; Chapter 4; University of Trieste: Trieste, Italy, 2012.
21. Ross, C.T.F. *Pressure Vessels—External Pressure Technology*, 2nd ed.; Woodhead Publishing: Cambridge, UK, 2011.
22. Ross, C.T.F.; Little, A.P.F.; Brown, G.X.; Saphiu, A. Buckling of near-perfect thick-walled circular cylinders under-external hydrostatic pressure. *J. Ocean Technol.* **2009**, *4*, 84–103.
23. Ross, C.T.F.; Little, A.P.F.; Short, D.; Brown, G. Inelastic buckling of geometrically imperfect tubes under external hydrostatic pressure. *J. Ocean Technol.* **2008**, 3, 75–90.
24. Kármán, T.V.; Tsien, H. The buckling of spherical shells by external pressure. *J. Aeronaut. Sci.* **1939**, *7*, 43–50. [CrossRef]
25. Hutchinson, J.W. Buckling of spherical shells revisited. *Proc. R. Soc. A Math. Phys. Eng. Sci.* **2016**, *472*, 20160577. [CrossRef]
26. Amiri, S.N.; Rasheed, H.A. Nondestructive method to predict the buckling load in elastic spherical shells. *Eng. Struct.* **2017**, *150*, 300–317. [CrossRef]
27. Rotter, J.M.; Mackenzie, G.; Lee, M. Spherical dome buckling with edge ring support. *Structures* **2016**, *8*, 264–274. [CrossRef]
28. Moon, C.J.; Kim, I.H.; Choi, B.H.; Kweon, J.H.; Choi, J.H. Buckling of filament-wound composite cylinders subjected to hydrostatic pressure for underwater vehicle applications. *Compos. Struct.* **2010**, *92*, 2241–2251. [CrossRef]
29. Kukulya, A.; Plueddemann, A.; Austin, T.; Stokey, R.; Purcell, M.; Allen, B.; Littlefield, R.; Freitag, L.; Koski, P.; Gallimore, E.; et al. Under-ice operations with a REMUS-100 AUV in the Arctic. In Proceedings of the IEEE/OES Autonomous Underwater Vehicles (AUV), Monterey, CA, USA, 1–3 September 2010.
30. Alvarez, A.; Caffaz, A.; Caiti, A.; Casilino, G.; Gualdesi, L.; Turetta, A.; Viviani, R. Fòlaga: A low-cost autonomous underwater vehicle combining glider and AUV capabilities. *Ocean Eng.* **2009**, *36*, 24–38. [CrossRef]
31. Carreras, M.; Candela, C.; Ribas, D.; Palomeras, N.; Magí, L.; Mallios, A.; Vidal, E.; Pairet, È.; Ridao, P. Testing SPARUS II AUV, an open platform for industrial, scientific and academic applications. In Proceedings of the Sixth International Workshop on Marine Technology, MARTECH, Cartagena, Spain, 15–17 September 2015.
32. Allotta, B.; Conti, R.; Costanzi, R.; Fanelli, F.; Gelli, J.; Meli, E.; Monni, N.; Ridolfi, A.; Rindi, A. A low cost autonomous underwater vehicle for patrolling and monitoring. *Proc. Inst. Mech. Eng. Part M J. Eng. Marit. Environ.* **2016**, *231*, 740–749. [CrossRef]
33. Det Norske Veritas. DNVGL-CG-0128 Class Guideline Buckling. 2015. Available online: http://www.dnvgl.com (accessed on 25 September 2019).
34. Ferri, G.; Ferreira, F.; Djapic, V. Multi-domain robotics competitions: The CMRE experience from SAUC-E to the European Robotics League Emergency Robots. In Proceedings of the IEEE OCEANS 2017, Aberdeen, Scotland, 19–22 June 2017; pp. 1–7.
35. Carlton, J. *Marine Propellers and Propulsion*, 2nd ed.; Butterworth-Heinemann Elsevier: Amsterdam, The Netherlands, 2007.
36. Fossen, T.I. *Guidance and Control of Ocean Vehicles*; John Wiley & Sons: Chichester, UK, 1994.

37. Von Mises, R.; Windenburg, D.F. *The Critical External Pressure of Cylindrical Tubes under Uniform Radial and Axial Load*; No. DTMB-366; David Taylor Model Basin: Washington, DC, USA, 1933.
38. BlueRobotics Tests. 2017. Available online: https://bluerobotics.com/new-products-aluminum-tubes/ (accessed on 23 March 2018).
39. Young, W.C.; Budynas, R.G. *Roark's Formulas for Stress and Strain*, 7th ed.; McGraw-Hill: New York, NY, USA, 2002.
40. Singer, J.; Arbocz, J.; Weller, T. *Buckling Experiments: Experimental Methods in Buckling of Thin-Walled Structures. Shells, Built-Up Structures, Composites and Additional Topics*; John Wiley & Sons: New York, NY, USA, 2002.
41. Det Norske Veritas. DNV CN30.1 Buckling Strength Analysis of Bars and Frames, and Spherical Shells. 2004. Available online: http://www.dnvgl.com (accessed on 25 September 2019).
42. Formatura di PLEXIGLAS®—Direttive per la lavorazione (Evonik Industries). Available online: https://www.plexiglas-shop.com/pdfs/it/311-2 (accessed on 18 April 2018).
43. Smith, P.; Błachut, J. Buckling of externally pressurized prolate ellipsoidal domes. *J. Press. Vessel Technol.* **2008**, *130*, 011210. [CrossRef]
44. Galletly, G.D.; Błachut, J.; Kruzelecki, J. Plastic buckling of imperfect hemispherical shells subjected to external pressure. *Proc. Inst. Mech. Eng. Part C J. Mech. Eng. Sci.* **1987**, *201*, 153–170. [CrossRef]